Sensitivity Analysis of the Lumped Thermal Model of the EU 170 GHz Gyrotron Magnetron Injection Gun

Carolina Introini, Nicolò Badodi, Ruggero Bertazzoni, Giuseppe Carannante, Jean-Philippe Hogge, Stefan Illy, Alberto Leggieri, Francisco Sanchez, Laura Savoldi, *Member, IEEE*, and Antonio Cammi, *Member, IEEE*

***Abstract*— The ITER Electron Cyclotron Resonance Heating and Current Drive (ECRH&CD) system relies on 1 MW 170 GHz Gyrotrons to provide the mm-wave power needed for plasma heating, current drive, and magneto-hydrodynamic control. The design and modeling of the control system of the Magnetron Injection Gun (MIG) is crucial to keep the emitter in the proper operating conditions. Within the MIG control system framework, a thermal lumped model has therefore been developed. As the MIG is characterized by a complex geometry and no temperature measurements of the system are available, parameters need to be introduced within the model, which must be optimized. This work presents a rigorous sensitivity analysis (SA) of the parameters of the MIG, intending to quantify the parameter effect on the model output to develop an ad hoc optimization algorithm. Both local and global SA will be discussed, with the latter specifically aiming at evaluating the inference between parameters. The subsequent optimization, which was carried out following the hierarchy of the parameters defined by the SA, will allow finding the optimal set of parameters for the lumped model of the MIG, which will then be validated against experimental data taken from outside those used for the analysis, proving the good results of the procedure and the determined parameter set.**

***Index Terms*— Current drive, lumped modeling, magnetron injection gun (MIG), optimization, sensitivity analysis (SA).**

I. Introduction

IN FUSION reactors, the plasma particles need external heating, typically provided by systems such as the Electron Cyclotron Resonance Heating and Current Drive (ECRH&CD) [1]. In ITER [2], this system will include 24 1 MW CW Gyrotrons operating at 170 GHz [3]: these devices must comply with high-level requirements to sustain long current pulses and work with total efficiency higher than 50%, whilst suppressing plasma instabilities. Since the occurrence of these instabilities is a priori unpredictable, the central system must be aware in real-time of the state of the ECRH&CD system to ask for action when required [4].

To ensure optimal control, the Gyrotrons of the ECRH&CD have been studied in detail [5]. Inside the Gyrotron, a 2 MW electron beam is generated from the Magnetron Injection Gun (MIG) through temperature-limited thermionic effect, which then interacts with a microwave cavity to allow the transfer of its energy into a high-frequency mode RF wave [6]. To ensure optimal operation, the physical conditions of the electron beam must be set with extreme precision within the nominal operational regime to avoid mode conversion and excitation of wrong modes and thus to avoid dissipating the full 2 MW electron beam [7]: this means that, within the MIG, the electron beam must be stabilized and any current drop must be limited, preferably using a suitable control system.

The MIG system is characterized by a complex geometry, shown in Fig. 1: to keep the electron beam uncontaminated by spurious emission from other components, the emitter temperature must be much higher than the other bodies within the MIG. For this purpose, thermal shields drive the input power toward the emitter whilst the central flowing oil removes the heat from the internal part of the system, keeping all components save for the emitter as cool as possible. As no temperature measurements of the system are available, models must be developed to study the MIG: for the implementation of the control system, which must act in real-time when

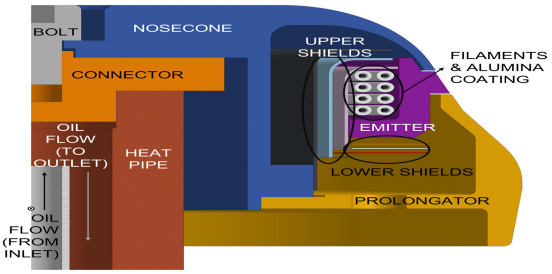

Fig. 1. CAD representation of the right upper half of the MIG.

Manuscript received 3 October 2023; accepted 29 November 2023. This work was supported by the EUROFusion Consortium under Grant 101052220 Views and opinions expressed are however those of the authors only and do not necessarily reflect those of the European Union or the European Commission. Neither entity can be held responsible for them. The review of this article was arranged by Senior Editor R. Chapman. *(Corresponding author: Antonio Cammi.)*

Carolina Introini, Nicolò Badodi, and Antonio Cammi are with the (Department of Energy, CeSNEF — Nuclear Engineering Division), Politecnico di Milan, 20156 Milan, Italy (e-mail: antonio.cammi@polimi.it).

Ruggero Bertazzoni and Francisco Sanchez are with the Fusion for Energy (F4E), 08019 Barcelona, Spain.

Giuseppe Carannante is with ITER Organization, 13115 Saint-Paul Lez Durance, France.

Jean-Philippe Hogge is with the Ecole Polytechnique Fédérale de Lausanne (EPFL), Swiss Plasma Center (SPC), 1015 Lausanne, Switzerland.

Stefan Illy is with the Institute for Pulsed Power and Microwave Technology (IHM), Karlsruhe Institute of Technology, 76344 Eggenstein-Leopoldshafen, Germany.

Alberto Leggieri is with THALES, Microwave and Imaging Sub-Systems, 78140 Vélizy-Villacoublay, France.

Laura Savoldi is with the Politecnico di Turin (MATHEP Group, Dipartimento Energia “Galileo Ferraris”), 10129 Turin, Italy.

Color versions of one or more figures in this article are available at https://doi.org/10.1109/TPS.2023.3348171.

Digital Object Identifier 10.1109/TPS.2023.3348171

required, high-fidelity 3-D models are too expensive from the computational point of view and they cannot be used in real-time scenarios. As such, this work makes use of a detailed physics-based lumped model based on the one developed in [8] and [9].

Due to the lack of experimental data and the high complexity of the system and the heat transfer mechanisms occurring between the MIG components, parameters must be introduced to close the equations that comprise the lumped model. These parameters are both physical (contact resistances between components) and "nonphysical", in the sense that they do not represent actual physical quantities but rather represent uncertainties and approximation in the model (such as physical uncertainties related to the thermionic effect and to the fast dynamics occurring on the emitter surface related to the electrons' emission). Regardless, the effect of these parameters on the beam current must be studied through a sensitivity analysis (SA), and subsequently optimized, as discussed in this work.

This work is structured as follows: Section II briefly summarizes the lumped model used in this work, along with the main beam current characteristics which are influenced by the model parameters; Section III discusses the approach and the results of the parameter SA; Section IV presents the results of the parameter optimization and subsequent model validation for selected pulses; finally, Section V, other than summarizing the obtained results, briefly discusses some future perspectives and planned analyses on this topic.

II. Lumped Thermal Model

Fig. 2 reports the equivalent electrical circuit representation of the MIG lumped model, developed in Python starting from [8], highlighting the unknown parameters to be optimized. Different colors of the equivalent thermal resistances indicate the different mechanisms of heat transfer that occur within the MIG. The key assumption behind lumped modeling is that each body of the system is characterized by a negligible temperature gradient, therefore each component can be described by a unique spatially uniform temperature varying in time. Compared to [8], all components are included in the present lumped model

The thermal dynamics of each body is obtained by means of the overall energy balance

$$mc\frac{dT}{dt} = q_{\text{in}} - q_{\text{out}} \tag{1}$$

where m is the mass of the body, c its specific heat capacity, T the temperature and q are the input and output transfer rate. Components that are in contact exchange heat through conduction (blue resistances R_k in Fig. 2)

$$q_k'' = \frac{T_1 - T_2}{R_{k,12}} \tag{2}$$

where $R_{k,12}$ is the contact resistance. The contact resistances [respectively, R_{pn}, R_{nc}, and R_{ch} for prolongator-nosecone, nosecone-connector and connector-heat pipe, as seen in Fig. 1)] are unknown physical parameters; for components within the inner and outer cavities, instead, conduction heat transfer is neglected since, due to the high temperatures of these bodies, the main heat transfer mechanism within the two cavities is radiative heat transfer

$$q_r'' = \frac{\sigma\left(T_1^4 - T_2^4\right)}{R_{r,12}} \tag{3}$$

where $R_{r,12}$ is the radiative heat resistance, which depends on the emissivity and the surface of the two bodies, and on the view factor between them (which indicates the portion of surface 1 seen by surface 2). Overall, the overall heat transfer within the cavities must satisfy the following:

$$q_k = \frac{E_{\text{bi}} - J_i}{R_{\text{ri}}} = \sum_{j=0}^{N} A_i F_{\text{ij}}\left(J_i - J_j\right) \tag{4}$$

where E_{bi} is the blackbody emission for body i, J_i is the radiosity flux, R_{ri} is the total surface resistance for body i, A_i is the surface exposed to the cavity, F_{ij} is the view factor between body i and body j, and N is the total number of bodies included in the cavity.

Convection heat transfer occurs between the oil and the solids in contact with it (the connector and heat pipe)

$$q_c'' = h(T_o - T_w) \tag{5}$$

where T_o is the oil temperature, T_w is the wall temperature and h is the convective heat transfer coefficient, computed using the Sieder-Tate and the Graetz-Nusselt correlations for, respectively, connector-to-oil and heat pipe-to-oil heat transfer coefficients.

The lumped temperature assumption for the emitter does not allow to catch the fast temperatures variations localized near the emitter surface: for this reason, the emitter thermal dynamic is divided into three different regions as shown in Fig. 2, so that the emitter surface can be described with a "fictitious" mass much smaller than that of the emitter body to allow faster response to surface temperature variations and better fit the experimental results. This leads to the introduction of four additional parameters.

1) Mass capacitances C_1 and C_2 describing the thermal inertia for the emitter intermediate and surface region.
2) Thermal resistances R_1 and R_2 describing the conductive resistance to heat transfer for the emitter intermediate and surface region.

The final parameter, C_B, is the *correction to beam* parameters, which includes the uncertainty related to the cooling effect of the emitter due to thermionic emission.

The nominal values for the eight parameters listed above were determined through a best fit of ten different training experimental pulses spanning the whole operational range (Section II-A), and are reported in Table I. The parameter range within which the SA has been performed has been set at $\pm 10\%$ the nominal value.

A. Pulse Features

A proper SA requires a primary analysis of the experimental data, aimed at finding out the most relevant features of the output and its possible correlations with different parameters of the real system. As such, the available experimental pulses

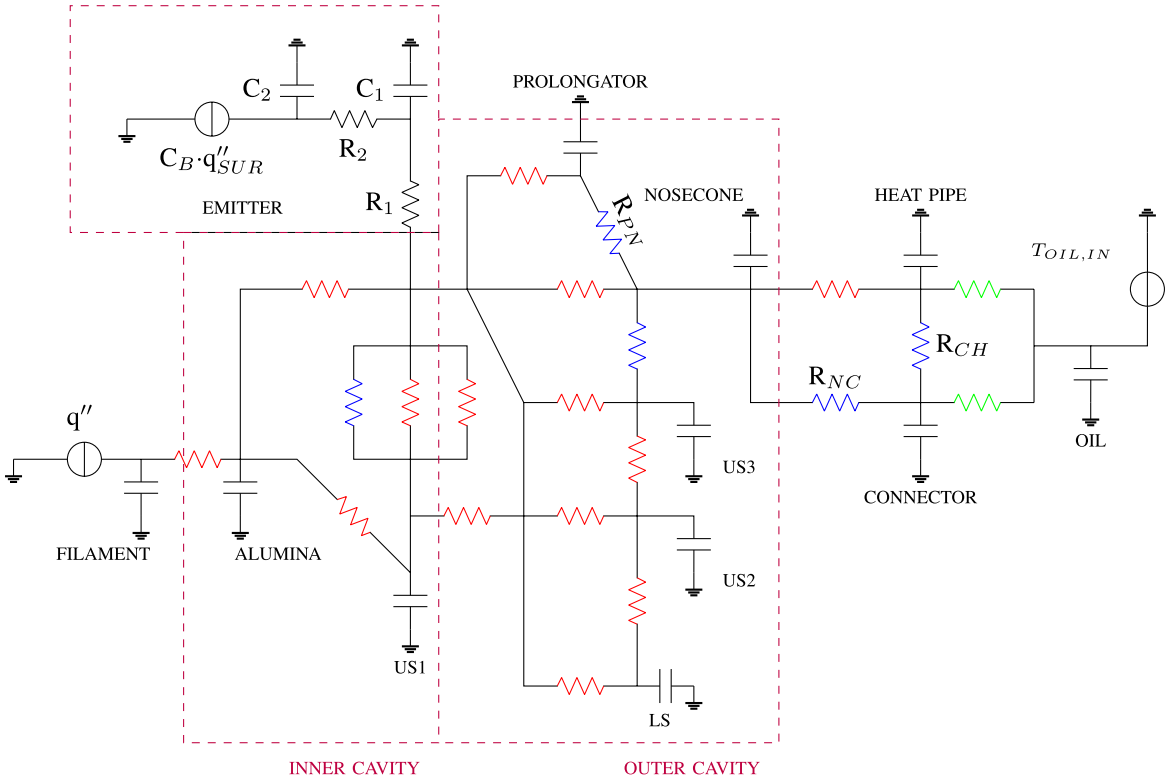

Fig. 2. Equivalent circuit representation of the MIG lumped model. Radiative resistances are in red; conduction resistances are in blue; convection resistances are in green.

TABLE I
NOMINAL PARAMETER SET

C_B	R_1	C_1	R_2	C_2	R_{pn}	R_{nc}	R_{ch}
0.48	0.173	116	0.184	24.76	0.157	0.88	1.201

from the FALCON Test facility at the Swiss Plasma Center (SPC), equipped with the TH1509U gyrotron prototype, were analyzed and organized depending on their characterizing parameters.

Figs. 3 and 4 report a typical non-optimized experimental pulse with its corresponding inputs, highlighting its main features that will be used for the sensitivity and the optimization analysis. In addition, Fig. 3 also highlights the unstable behavior of the current once the pulse starts: the beam current varies by 5.56 A (10.57% of the final current reached by the beam). The pulse starts when the gyrotron is in the so-called "on-phase", with the filament power and the cathode voltage turned on: this leads to an increase of the filament and thus of the emitter temperature, which leads to current emission by thermionic effect.

Each experimental pulse is characterized by the following.

1) Pulselength $L \in [60 - 300]$ s.
2) Filament input power $P_I \in [330 - 375]$ W.
3) Accelerative voltage $V_{A0} \in [68 - 75]$ kV.

During the beam current emission, key pulse features can be identified, upon which the SA will focus.

1) Initial peak $I_{\text{PEAK}} = f(V_A, P_I)$, which corresponds to the activation of the accelerative voltage, and depends on accelerative voltage and initial temperature of the emitter surface (which depends on the input power).
2) Power boost $P_{\text{MAX}} \in [540 - 770]$ W, to minimize the cooling effect of the cathode and thus the current drop.
3) Beam current drop I_{MIN}, caused by the cooling effect of the cathode due to thermionic emission.
4) Step voltage increase $V_{A1} \in [70 - 75]$ kV.
5) Beam current final value I_F, which usually lies around 50 A and depends on the input power and the pulse duration.

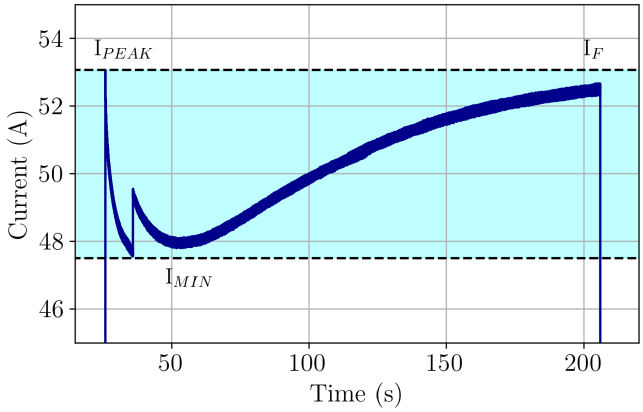

Fig. 3. Key pulse features, highlighting the peak current, the minimum current reached during the drop, and the final current.

III. SENSITIVITY ANALYSIS

The SA is carried out using the one at time (OAT) approach and the variance based analysis (VBA) to identify

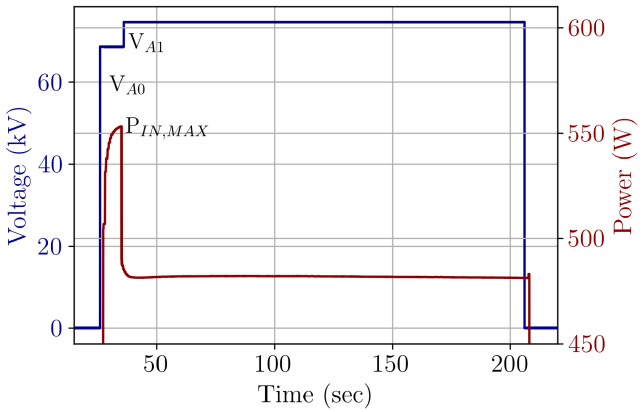

Fig. 4. Input quantities for the pulse: filament power (red) and accelerative voltage (blue).

the parameters that have the greatest effect on the model [10]. In the OAT approach, only one parameter is varied at each simulation within the parameter range cited in Section II, whereas all other types of information and the other parameters are fixed so that they cannot cause variation in the model response. Once each simulation is completed, the variable parameter returns to its nominal value.

In general, the model output Y, given the k parameters $\{x_r\}_{r=1,k} = X_1, X_2, \ldots, X_k$ and under the approximation that each parameter is independent of the others and provides a linear effect on the output, can be computed as follows:

$$Y = b_0 + \sum_{r=1}^{k} b_r X_r \tag{6}$$

where b_0 are unknown constant values. Sensitivity indexes can be measured by monitoring changes in the model output between the various simulations, and thanks to the OAT approach any change in the output between Y_i and Y_{i+1} is unambiguously attributed to the single variable changed X_i. For example, through VBA it is possible to compute the Sobol indices of each parameter, decomposing the variance of the model output into fractions, each attributed to specific inputs. VBA allows to identify both parameters which account for the most of output variation, and therefore should be optimized with higher priority and parameters with no significant contribution to the model output, which therefore can be fixed without affecting the output variance.

The response Y can thus be decomposed as follows:

$$Y = f(X_1, X_2, \ldots, X_k). \tag{7}$$

Then, considering an expansion of f in terms of increasing dimension

$$f = f_0 + \sum_i f_i + \sum_i \sum_{j>1} f_{ij} + \cdots + f_{12,\ldots,k} \tag{8}$$

each term of the expansion, which is a function only of the factors in its index, can be univocally calculated using the expectation of the model output Y (provided that they have zero mean)

$$f_i = E(Y|X_i) - E(Y). \tag{9}$$

TABLE II
SOBOL INDEXES FOR THE EIGHT MODEL PARAMETERS

	$S_1\ I_{PEAK}$	$S_1\ I_F$	$S_1\ I_{MIN}$	$S_1\ I_{GLOBAL}$
C_B	0	0.74	0.69	0.83
R_1	0	0.16	0	0.11
C_1	0	0.06	0.03	0.01
R_2	0	0.04	0.25	0.05
C_2	0	0	0.03	0
R_{pn}	0.37	0	0	0
R_{nc}	0.42	0	0	0
R_{ch}	0.21	0	0	0

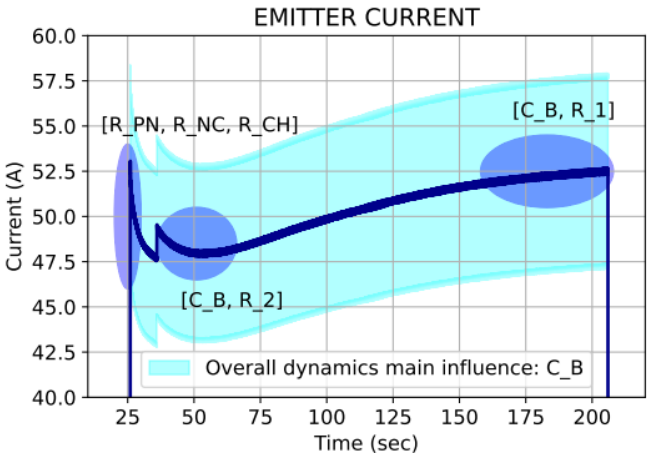

Fig. 5. Main results of the SA, highlighting the effect of the parameters on the pulse.

The variances of the terms of (9) are the measure of importance being sought, and they take the form

$$V(f_i(X_i)) = V(E(Y|X_i)). \tag{10}$$

Then, dividing by the unconditional variance $V(Y)$, the first order sensitivity index for each parameter can be computed as follows:

$$S_i = \frac{V(E(Y|X_i))}{V(Y)}. \tag{11}$$

Table II summarizes the Sobol indexes for the eight parameters, whereas Fig. 5 shows the influence of the parameters on the key pulse features described in Section II-A. The contact resistances of the components external to the cavity (prolongator, nosecone, connector, and heat pipe) strongly influences the initial current peak, whereas they hold no influence over the overall dynamic of the pulse. From the physical point of view, the initial peak strongly depends on the initial temperatures of the various components of the MIG, and not on the dynamics of the emitter. Conversely, the current drop and the final current value are influenced mainly by the correction to beam factor and by the emitter resistances, that is, the heat conduction within the emitter, from the surface that sees the filaments to the outer one from where electrons are emitted, thus justifying the choice of modeling the emitter with three different regions instead as a lumped body. Overall, the

main influence on the MIG dynamics is given by the parameter C_B, that is, the uncertainty related to the thermionic effect and thus the cooling effect due to electrons' emission.

From this analysis, is clear that the contact resistances must be optimized first before any other estimation is made. Then, the other parameters can be optimized following the ranking given by the Sobol indexes (first C_B, then the emitter resistances, then the emitter capacitances, the latter two having almost negligible effect on the beam current).

IV. Parameter Optimization

The optimization goal is to find the parameter set that minimizes the least square error between model output and experimental beam current for the largest number of input pulses. The optimization is built from the results of the SA of Section III. Given the vector of unknown parameters p, the optimization problem for the present case is defined as follows:

$$\min_p f_0(p) \in \left[0.9 \cdot p : 1.1 \cdot p\right] \tag{12}$$

where p is the vector of unknown parameters, f_0 is the objective function (in this case, the least square error between model output and experimental beam current). For the present optimization problem, no constraints are needed. Then, p^* is the optimum set of parameters such that

$$\forall z : f_0(z) \geq f_0\left(p^*\right), \quad p^* \in \left[0.9 \cdot p : 1.1 \cdot p\right]. \tag{13}$$

As mentioned in Section III, first the contact resistances are estimated by minimizing the error between the predicted and experimental values of the initial peak I_{PEAK}, keeping the other parameters at their nominal value. The optimization is carried out using the Differential Evolution (DE) algorithm using short pulses (pulselength L $<$ 10 s) independent of other pulses, which means that the time between two consecutive pulses is such that the emitter temperature has reached the new equilibrium state following the end of the first pulse, so that the initial conditions of the second pulse can be well-defined. From experiments, this is achieved by distancing the pulses by at least 10 min. The results of this optimization are shown in Fig. 6 for the prolongator-nosecone resistance R_{pn}: the other two parameters (R_{cn} and R_{ch}) show similar behavior, and thus are omitted here for sake of brevity. From the optimization, the combination of values that best minimize the error on I_{PEAK} have been selected as optimum values for the three contact resistances, namely $R_{\mathrm{pn}} = 0.175$, $R_{\mathrm{nc}} = 0.896$, $R_{\mathrm{ch}} = 1.206$ (all values have standard deviation lower than 0.2).

Following the optimization of the contact resistances, the rest of the parameters are now optimized in the order defined by the SA. For these parameters, independent long pulses (pulselength L $>$ 10 s) are used to track the parameters' effect on the overall dynamic of the beam current. The objective function for this second optimization is the Root Mean Square Error (RMSE) between model prediction and experimental beam current

$$\mathrm{RMSE} = \sqrt{\frac{\int_0^N \left(I_{\mathrm{MODEL}}(t) - I_{\mathrm{EXP}}(t)\right)^2 dt}{N}} \tag{14}$$

where N is the length of the pulse.

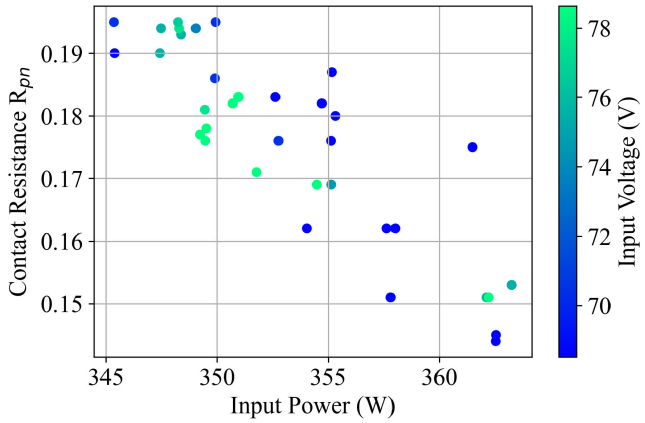

Fig. 6. Results of the DE algorithm for R_{pn}, for different input power and voltage within the operational range.

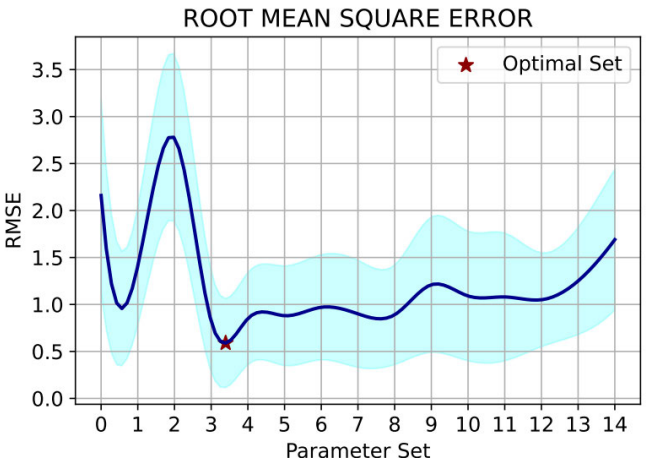

Fig. 7. Average RMSE for the long pulse dataset for the different optimal parameter sets.

A local optimization algorithm is used, whose result is shown in Fig. 7: for each pulse, the optimal parameter set is computed; then, each one of these optimal sets is used as parameter value for all other pulses, thus computing for each optimal set an average RMSE which takes into account all long pulses of the dataset. The parameter values corresponding to the minimum average RMSE are taken as optimal values for the whole dataset, highlighted in red on Fig. 7 (which means that the optimal set 3 is the one with the lower average RMSE considering all pulses in the dataset, not only the one for which this set is the actual optimum one). These values are as follows: $C_B = 0.44$, $R_1 = 0.18$, $C_1 = 117$, $R_2 = 0.12$, $C_2 = 18.9$.

To test the accuracy of the SA and the optimization carried out, the optimal set of parameters previously defined has been set in the model and used to simulate two long pulses not present in the optimization dataset. Fig. 8 reports the results of this validation, showing how the optimized model is successful in correctly capturing both the local features of the pulse (initial peak, current drop, accelerating voltage step, final current value) but also the global dynamic of the beam current, thus confirming the good performances of the optimized model and the accuracy of the optimization procedure.

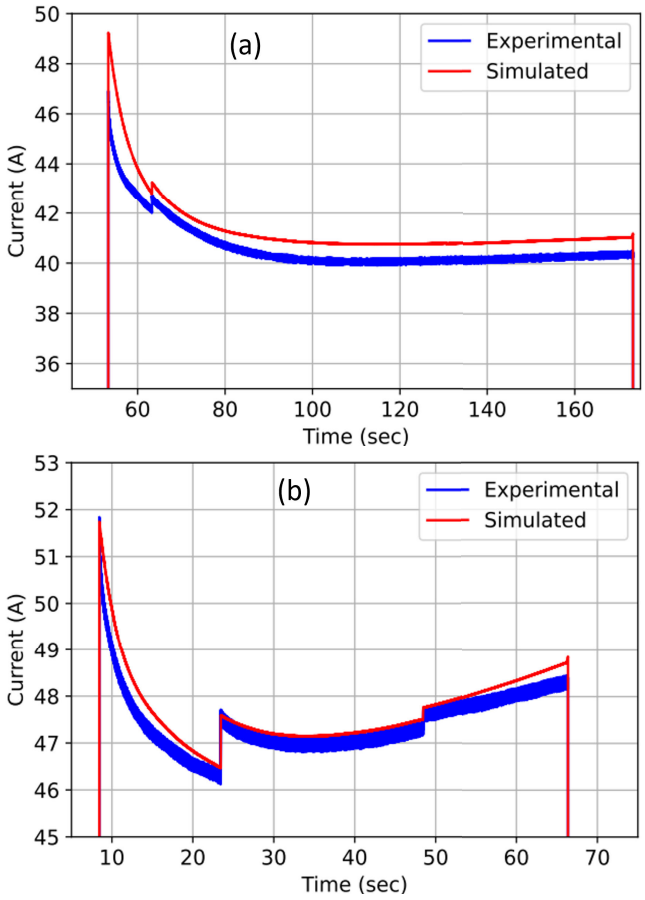

Fig. 8. Model validation for two long pulses not included in the optimization dataset.

V. Conclusion

The SA performed on the lumped MIG model allowed to understand whose model parameters and thus whose physical quantities affect the beam current emission: 1) the initial temperature of the external components influence the initial peak current; 2) the internal dynamic of the emitter, and in particular the internal heat conduction from the surface exposed to the filaments to the external one, influences the overall beam current emission; and 3) the uncertainty related to the thermionic effect has the largest influence on the beam current, indicating that more studies on this phenomenon are needed.

Following the SA, a parameter optimization was carried out in two steps: 1) through a DE, the contact resistances were optimized to the initial current peak; and 2) then, a local optimization algorithm was used for the rest of the parameters using as objective function the average RMSE over all long pulses in the optimization dataset. The optimal set of parameters was then tested by simulating two long pulses outside the optimization dataset: the good results of this validation step confirmed the accuracy of the procedure and the good performance of the lumped model in predicting the beam current.

Future studies will be devoted on the optimization and characterization of multiple pulses in sequence, thus losing the independence assumption between consecutive pulses. Following this, a control system for the filament current to stabilize the beam current emission and limiting the initial drop will be carried out, using both a feed-forward and a feedback approach. Concurrently, 3-D modeling of the MIG will be finalized.

Disclaimer

This work results from a collaboration with Thales, the EU Fusion Laboratories, SPC, F4E, and the ITER Organization. The views expressed in this publication are the sole responsibility of authors and do not necessarily reflect the views of F4E, the European Commission or the ITER Organization.

References

[1] ITER. *External Heating System*. Accessed: May 30, 2022. [Online]. Available: http://www.iter.org/mach/heating

[2] [Online]. Available: http://www.iter.org

[3] M. Q. Tran and P. Agostinetti, "Status and future development of heating and current drive for the EU DEMO," *Fusion Eng. Des.*, vol. 180, Jan. 2022, Art. no. 113159, doi: 10.1016/j.fusengdes.2022.113159.

[4] THALES Group. (2018). *ITER and Heating Systems in Tokamaks*. [Online]. Available: https://www.thalesgroup.com/en/iter-and-heating-systems-tokamaks

[5] A. Leggieri et al., "Progress of European industrial gyrotron developments for nuclear fusion," in *Proc. 24th Int. Vac. Electron. Conf. (IVEC)*, Chengdu, China, Apr. 2023, pp. 1–2.

[6] G. Gantenbein, "Reactor progress in the development of the European 1 MW 170 GHz CW gyrotron for ITER," in *Proc. 27th IAEA FEC Conf.*, 2018.

[7] F. Wilde et al., "Automated mode recovery for gyrotrons demonstrated at Wendelstein 7-X," *Fusion Eng. Des.*, vol. 148, Nov. 2019, Art. no. 111258, doi: 10.1016/j.fusengdes.2019.111258.

[8] N. Badodi, A. Cammi, A. Leggieri, F. Sanchez, and L. Savoldi, "A new lumped approach for the simulation of the magnetron injection gun for MegaWatt-class EU gyrotrons," *Energies*, vol. 14, no. 8, p. 2068, Apr. 2021, doi: 10.3390/en14082068.

[9] C. Introini, N. Badodi, A. Collaku, F. Timperi, L. Savoldi, and A. Cammi, "Numerical modelling and verification of the magnetron injection gun of the European 1MW 170 GHz Gyrotron," *IEEE Access*, to be published.

[10] A. Saltelli, *Global Sensitivity Analysis*. Hoboken, NJ, USA: Wiley, 2008.